

Article

Dimethyl Ether to Olefins on Hybrid Intergrowth Structure Zeolites

Maria V. Magomedova^{1,2,*} , Anastasiya V. Starozhitskaya¹ , Ilya A. Davidov¹, Dmitry E. Tsaplin^{1,3} and Anton L. Maximov¹ 

¹ A.V. Topchiev Institute of Petrochemical Synthesis, RAS (TIPS RAS), 29 Leninsky Prospekt, 119991 Moscow, Russia

² Lomonosov Institute of Fine Chemical Technologies, Russian Technological University (MIREA), 86 Vernadsky Prospekt, 119454 Moscow, Russia

³ Faculty of Chemistry, Lomonosov Moscow State University, 1 Leninskie Gory Str., 119234 Moscow, Russia

* Correspondence: podlesnaya@ips.ac.ru

Abstract: A series of catalysts based on hybrid intergrowth structure zeolites MFI-MEL, MFI-MTW, and MFI-MCM-41 are studied in the reaction of olefins synthesis from dimethyl ether at atmospheric pressure and a temperature of 340 °C. The total acidity of hybrid zeolite-based catalysts is shown to correlate with their activity. However, the use of zeolite with the structure MFI-MCM-41, which is characterized by a high content of medium acid sites, additionally catalyzes the methanol dehydration reaction, resulting in a decrease in the observed DME conversion. The obtained product distributions are brought into correlation with the texture of catalysts. It is shown that the use of hybrid zeolites does not change the mechanism of reaction, but the structural features of zeolites influence the priority of the competing MTO reactions: high ethylene yield is observed for catalysts with high micropore volume. The topology of the hybrid zeolite has been shown to influence the hydrogen transfer reaction rate, but not to change the isomerizing activity of the catalyst.

Keywords: hybrid zeolites; intergrowth structure; MTO reaction; dimethyl ether; light olefins; MEL; MTW; MCM-41; MFI



Citation: Magomedova, M.V.; Starozhitskaya, A.V.; Davidov, I.A.; Tsaplin, D.E.; Maximov, A.L. Dimethyl Ether to Olefins on Hybrid Intergrowth Structure Zeolites. *Catalysts* **2023**, *13*, 570. <https://doi.org/10.3390/catal13030570>

Academic Editor: Narendra Kumar

Received: 7 February 2023

Revised: 9 March 2023

Accepted: 10 March 2023

Published: 11 March 2023



Copyright: © 2023 by the authors. Licensee MDPI, Basel, Switzerland. This article is an open access article distributed under the terms and conditions of the Creative Commons Attribution (CC BY) license (<https://creativecommons.org/licenses/by/4.0/>).

1. Introduction

The reaction of oxygenates (methanol and dimethyl ether) to light olefins occurs with the involvement of microporous catalysts based on MFI zeolite or CHA silicoaluminophosphate [1–4]. A large number of studies using solid-state NMR spectroscopy, a pulse reactor, and the reaction with labeled ¹³C atoms have been conducted to determine the MTO (methanol-to-olefins) reaction mechanism [5–11]. Despite the different structural characteristics of MFI and CHA microporous materials, the reaction is considered to follow a dual-cycle mechanism, which was proposed by a group of Norwegian researchers in 2007 [12–14]. This mechanism was subsequently confirmed by both theoretical studies and a number of experimental observations [15–24]. According to this mechanism, in the first step, hydrocarbon pool species (aromatic cations, alkyl cyclopentyl cations) are formed in the micropores of the catalyst. Then, hydrocarbon pool species contact with reagents and semi-products in a series of parallel methylation and dealkylation reactions to form light olefins. The resulting products participate in oligomerization, isomerization, and H-transfer reactions to form higher olefins, aromatic compounds, and alkanes [15,23,25,26]. Hydrocarbon pool species act as an organic catalyst for the conversion of oxygenates into hydrocarbons, while Lewis and Brønsted acid sites of zeolite or silicoaluminophosphate stabilize hydrocarbon pool species in micropores. Moreover, due to the molecular-sieve properties, the structure of zeolite or silicoaluminophosphate determines product selectivity.

However, the catalysts used in the MTO reaction are characterized by a low diffusion coefficient of the molecules inside the zeolite or silicoaluminophosphate micropores [27,28].

The low diffusion rate of the reagents to the active sites leads to a decrease in the activity of the catalyst, while the low diffusion rate of the reaction products from the micropores leads to active secondary reactions, a decrease in the selectivity of target products, and rapid catalyst deactivation [29–34].

To improve mass transfer, micro-mesoporous catalysts are used. In the case of MFI-type zeolite, they can be obtained by mixing it with mesoporous materials (Al_2O_3 , clay, galloisite) or by posttreatment with alkali or acid, removing silicon or aluminum atoms from the framework of the crystal lattice and forming the hierarchical structure [35–39]. The use of such catalysts reduces steric difficulties and increases the diffusion rate of reagents and products, which, in turn, leads to increased activity.

An alternative method of forming MFI-type zeolites with micro- and mesopores is the synthesis of hybrid zeolites—co-crystallites, which, in addition to the MFI structure, contain the structure of the other microporous material. Mesopores are formed directly during synthesis by the formation of additional cavities at the intersections of the channels and/or interparticle voids of zeolites [40–43]. Such hybrid zeolites in the reaction of hydrocarbon synthesis from oxygenates have not been sufficiently investigated [42–44].

In this paper, we conducted a study of the influence of textural and acid properties of micro- and mesoporous structure catalysts based on hybrid zeolites MFI-MEL/ Al_2O_3 , MFI-MTW/ Al_2O_3 , and MFI-MCM-41/ Al_2O_3 on the distribution of reaction products in the synthesis of light olefins from DME. The results were compared with the standard catalyst MFI/ Al_2O_3 , which was studied in [45].

2. Results and Discussion

2.1. Characterization of the Catalysts

The characterization of hybrid zeolites is presented in Supplementary Materials (Table S1. Phase ratio, Si/Al ratio; Figure S1. ^{27}Al MAS NMR spectra; Figure S2. IR spectra of pyridine adsorbed on hybrid zeolites; Table S2. The distribution of Lewis and Brønsted acid sites; Figure S3. SEM and TEM micrographs).

According to XRD patterns of the catalysts, all samples contain the MFI topology structure, as evidenced by the presence of specific-to-MFI reflections at $2\theta = 7.9, 8, 23.2, 23.9, \text{ and } 24.4^\circ$ [46] (Figure 1A).

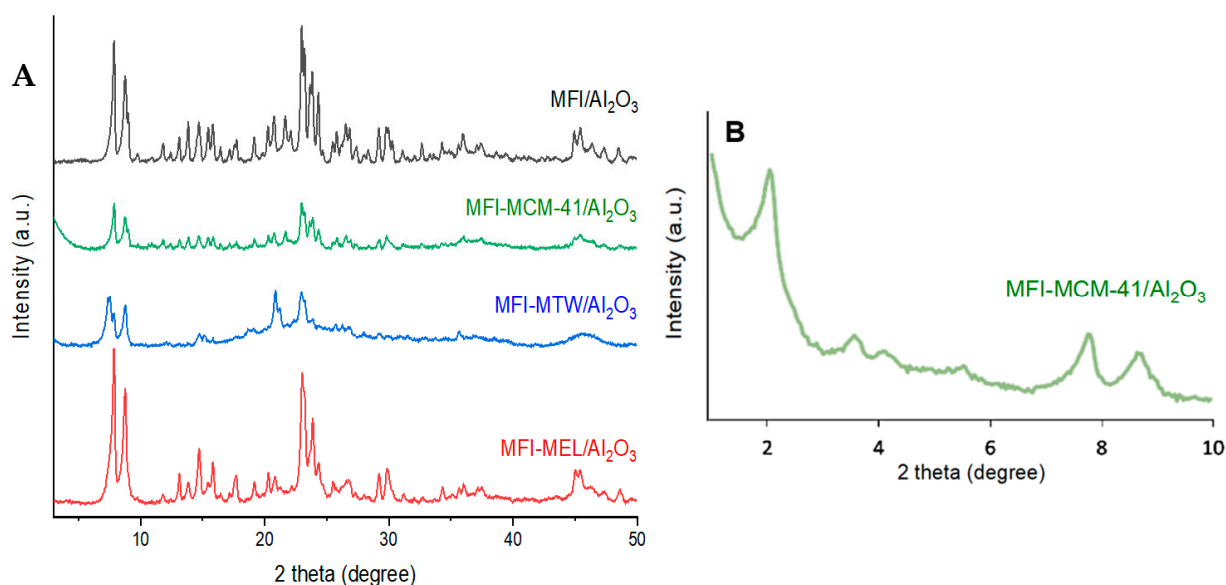


Figure 1. XRD patterns of the catalysts. (A) WAXRD-patterns; (B) SAXRD-pattern of MFI-MCM-41/ Al_2O_3 .

The presence of the MEL structure in the MFI-MEL/ Al_2O_3 sample is confirmed by the presence of reflections at $2\theta = 7.92, 8.78, 23.14, 23.98,$ and 45.2° [47]. The MFI-MTW/ Al_2O_3 catalyst XRD pattern contains reflections that are characteristic of the MTW type structure at $2\theta = 7.2, 8.8, 20.7,$ and 23.1° [48]. The presence of MCM-41 in the MFI-MCM-41/ Al_2O_3 catalyst is confirmed by the characteristic reflection of the amorphous SiO_2 of MCM-41 at $2\theta = 22.8^\circ$ and the reflection at $2\theta = 2.2^\circ$ on the small-angle X-ray diffraction pattern (Figure 1B) [40].

Quantification of the hybrid zeolite phase ratio can be performed through an assessment of the contribution of different structures to the final XRD pattern [49]. On the catalysts MFI-MEL/ Al_2O_3 and MFI-MTW/ Al_2O_3 , the zeolite phase ratio is 55/45 and 60/40, respectively [50]. The MFI/MCM-41 ratio is 80/20. All hybrid zeolites have an intergrowth structure and do not contain crystallites of individual phases, which is confirmed by SEM and TEM micrographs (Supplementary Materials Figure S3).

Table 1 shows the texture properties of the samples. External surface areas, micro- and mesopore surface areas, and the average diameters of micro- and mesopores for all catalysts are presented in Supplementary Materials (Table S3).

Table 1. Textural properties of the MFI-MEL/ Al_2O_3 , MFI-MTW/ Al_2O_3 , MFI-MCM-41/ Al_2O_3 samples.

No	Catalyst	$S_{\text{BET}}, \text{m}^2/\text{g}(\text{Cat})$	$S_{\text{micro}}, \text{m}^2/\text{g}(\text{Cat})$	$V(\text{pore}), \text{cm}^3/\text{g}(\text{Cat})$		
				Total	Micro	Meso
1	MFI-MEL/ Al_2O_3	361	250	0.286	0.088 (30.8%)	0.198 (69.2%)
2	MFI-MTW/ Al_2O_3	179	11	0.443	0.012 (2.7%)	0.431 (97.3%)
3	MFI-MCM-41/ Al_2O_3	250	42	0.340	0.040 (11.8%)	0.300 (88.2%)
4	MFI/ Al_2O_3	293	181	0.198	0.057 (28.7%)	0.142 (71.3%)

Catalysts based on hybrid zeolites MFI-MEL, MFI-MTW, and MFI-MCM-41 have a significantly larger mesopore volume ($0.198\text{--}0.431 \text{ cm}^3/\text{g}$) than the standard catalyst based on MFI zeolite ($0.142 \text{ cm}^3/\text{g}$).

The hybrid zeolite-based catalyst MFI-MEL/ Al_2O_3 is characterized by the largest specific surface area among the studied samples— $361 \text{ m}^2/\text{g}$, the average total pore volume— $0.286 \text{ cm}^3/\text{g}$, and, at the same time, the largest micropore volume— $0.88 \text{ cm}^3/\text{g}$ (30.8%).

The hybrid zeolite-based catalyst MFI-MTW/ Al_2O_3 is characterized by the smallest specific surface area— $179 \text{ m}^2/\text{g}$, and the largest total pore volume— $0.443 \text{ cm}^3/\text{g}$, while it almost does not have micropores—their volume is $0.012 \text{ cm}^3/\text{g}$ (2.7%). The large total pore volume of the MFI-MTW/ Al_2O_3 catalyst is created by mesopores, which have a volume of $0.431 \text{ cm}^3/\text{g}$.

The MFI-MCM-41/ Al_2O_3 catalyst is characterized by an average specific surface area of $250 \text{ m}^2/\text{g}$, which is slightly lower than for the standard MFI/ Al_2O_3 sample, but higher than for the catalyst based on the MFI-MTW/ Al_2O_3 hybrid zeolite. This sample is in the middle in relation to the total pore volume— $0.340 \text{ cm}^3/\text{g}$, and the micropore volume— $0.040 \text{ cm}^3/\text{g}$ (11.8%).

In terms of the reaction mechanism, MFI-MEL/ Al_2O_3 should be considered the most promising sample, which has the largest volume of micropores necessary for stabilizing hydrocarbon pool species.

The results of the analysis of the ammonia TPD spectra for the samples are shown in Figure 2. It should be noted that the acidity determined by TPD NH_3 can be overestimated; however, these values can be compared with each other with a high degree of confidence. The TPD spectra are resolved to Gaussian peaks using the Peak Deconvolution tool of the Origin 2018 software package [51,52].

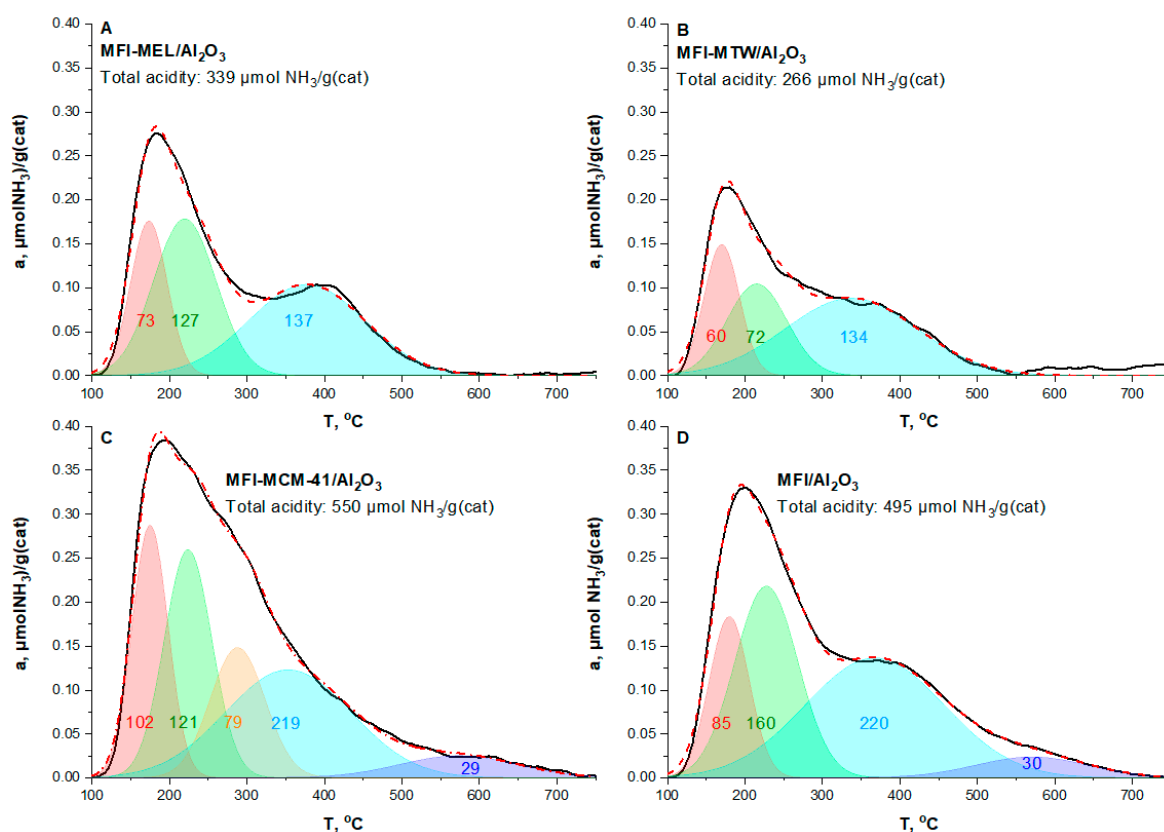


Figure 2. NH_3 -TPD profiles of ammonia: (A) MFI-MEL/ Al_2O_3 , (B) MFI-MTW/ Al_2O_3 , (C) MFI-MCM-41/ Al_2O_3 , (D) MFI/ Al_2O_3 and their deconvolution into Gaussian peaks. The black solid line is the experimental curve. The red dotted line is the cumulative curve of Gaussian peaks. Numbers indicate the amount of acid sites corresponding to the peak, $\mu\text{mol NH}_3/\text{g}(\text{cat})$.

For all samples, there are two peaks of ammonia desorption at the temperatures of 170–180 °C and 215–230 °C that correspond to the aluminum oxide and zeolite weak Lewis acid sites such as AlO^+ or charged $\text{Al}_x\text{O}_y^{n+}$ clusters, respectively [53].

All samples are characterized by the desorption peak at the temperature of 350–380 °C. These peaks correspond to strong Brønsted acid sites represented by bridging OH^+ groups.

For the MFI-MCM-41/ Al_2O_3 and the standard MFI/ Al_2O_3 , superacid sites are observed at a desorption temperature of 570 °C. These peaks correspond to strong Lewis acid sites—extraframework aluminum atoms [53–57].

For MFI-MCM-41/ Al_2O_3 , there is no pronounced local minimum between the peaks of weak 170–180 °C and strong 350–380 °C acid sites in the TPD spectra, and a peak at the desorption temperature of 290 °C can be observed at deconvolution. This peak corresponds to the Brønsted acid sites of medium strength—the OH-group located on tetrahedral embedded aluminum atoms in the structure MCM-41 [58–62]. As the unmodified MCM-41 has no aluminum in the lattice, the observed medium-strength Brønsted acid sites confirm the formation of a hybrid structure MFI-MCM-41/ Al_2O_3 [63].

The centers of the peaks corresponding to the weak and strong acid sites on different samples are slightly shifted along the temperature axis (within 10–30 °C), which is most likely due to the different diffusion restrictions on different zeolite structures [53].

The total acidity of samples decreases in the series MFI-MCM-41/ Al_2O_3 > MFI/ Al_2O_3 > MFI-MEL/ Al_2O_3 > MFI-MTW/ Al_2O_3 and is 550, 495, 339, and 267 $\mu\text{mol NH}_3/\text{g}(\text{cat})$, respectively. Numerical values of acidity for samples are presented in Table 2.

Table 2. Acidic properties of catalysts.

No	Sample	Acidity of Fresh Catalyst, $\mu\text{mol NH}_3/\text{g}(\text{cat})$				
		Total	Weak Sites	Medium Sites	Strong Sites	
			$T_1 = 170\text{--}180\text{ }^\circ\text{C}$ $T_2 = 215\text{--}230\text{ }^\circ\text{C}$	$T_3 = 290\text{ }^\circ\text{C}$	$T_4 = 350\text{--}380\text{ }^\circ\text{C}$	$T_5 = 570\text{ }^\circ\text{C}$
1	MFI-MEL/ Al_2O_3	339	200 (59.0%)	-	139 (41.0%)	-
2	MFI-MTW/ Al_2O_3	266	132 (49.6%)	-	134 (50.4%)	-
3	MFI-MCM-41/ Al_2O_3	550	223 (40.5%)	79 (14.4 %)	219 (39.8%)	29 (5.3%)
4	MFI/ Al_2O_3	495	245 (49.5%)	-	220 (44.4%)	30 (6.0%)

2.2. DME Conversion to Olefin

The dependence of DME conversion on the specified contact time for the samples studied is shown in Figure 3A. For all catalysts, the DME conversion increases with an increase in specified contact time. The resulting pattern of dependences can be described by an S-shaped curve, which reflects the autocatalytic nature of the MTO reaction [25,64].

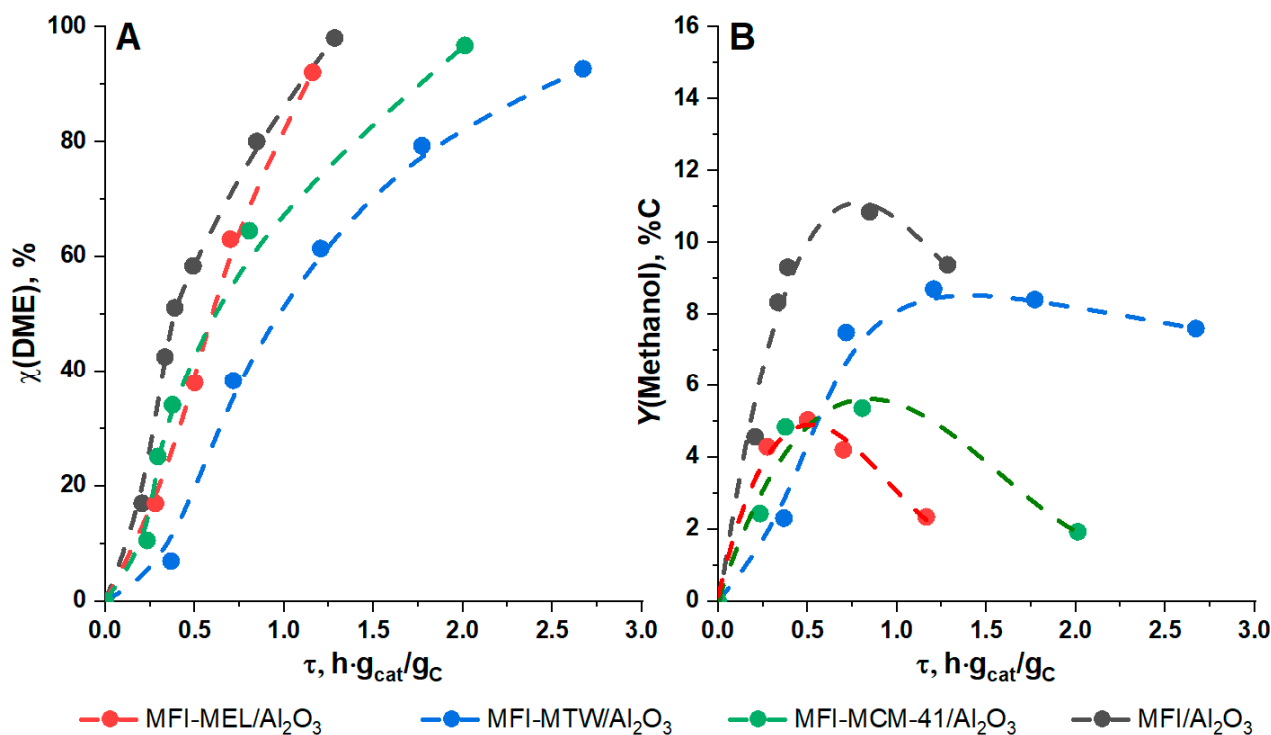


Figure 3. DME conversion (A) and methanol yield (B) as functions of specified contact time. $p = 1$ atm, $T = 340\text{ }^\circ\text{C}$.

The activity of the studied catalysts decreases in the series $\text{MFI}/\text{Al}_2\text{O}_3 > \text{MFI-MEL}/\text{Al}_2\text{O}_3 > \text{MFI-MTW}/\text{Al}_2\text{O}_3$, which correlates with the total acidity of these samples: $495 > 339 > 266\ \mu\text{mol NH}_3/\text{g}(\text{cat})$.

At the same time, the sample based on the zeolite MFI-MCM-41/ Al_2O_3 , which is characterized by the highest total acidity of $550\ \mu\text{mol NH}_3/\text{g}(\text{cat})$, stands out from this sequence. The dependence of the DME conversion on the specified contact time for the MFI-MCM-41/ Al_2O_3 catalyst lies below the analogous curve for the MFI/ Al_2O_3 standard sample. Furthermore, on the MFI-MCM-41/ Al_2O_3 sample, there is a significant decrease in the yield of methanol compared to the standard MFI/ Al_2O_3 sample (Figure 3B). This is due to the fact that medium-strength acid sites (in the amount of $79\ \mu\text{mol NH}_3/\text{g}(\text{cat})$) of MCM-41 do not participate in the reaction of hydrocarbon synthesis from oxygenates, but

activate the dehydration of methanol with the formation of DME, as was shown in [65,66]. Therefore, for the sample based on the MFI-MCM-41 zeolite, not only are hydrocarbons formed due to the structure of the MFI, but the additional formation of the DME from methanol also occurs due to the presence of MCM-41.

On the MFI-MEL/ Al_2O_3 catalyst, at low specified contact times (up to $0.25 \text{ h}\cdot\text{g}(\text{cat})/\text{g}(\text{C})$), the DME conversion is lower than that of the standard MFI/ Al_2O_3 sample. At specified contact times of more than $0.5 \text{ h}\cdot\text{g}(\text{cat})/\text{g}(\text{C})$, the DME conversion increases sharply and, at $1.2 \text{ h}\cdot\text{g}(\text{cat})/\text{g}(\text{C})$, it is close to DME conversion on MFI/ Al_2O_3 .

The MFI-MEL/ Al_2O_3 sample is characterized by the largest micropore volume ($0.088 \text{ cm}^3/\text{g}$). Micropores of zeolite are associated with the formation and stabilization of hydrocarbon pool species such as aromatic and polymethylcyclopentyl cations. The rate of this stage is low; therefore, an induction period is observed on the DME conversion curve at small specified contact times. However, when the hydrocarbon pool is already formed, it can be seen that DME conversion on MFI-MEL/ Al_2O_3 increases sharply.

The interrelation between the micropores volume of the catalyst and its catalytic properties can be seen in the dependence of the methanol yield on the DME conversion. The maximum yield of methanol decreases in the series MFI-MTW/ $\text{Al}_2\text{O}_3 > \text{MFI-MCM-41}/\text{Al}_2\text{O}_3 > \text{MFI-MEL}/\text{Al}_2\text{O}_3$ (Figure 3B). The minimum yield of methanol (5.0% C) is observed on MFI-MEL/ Al_2O_3 , while the maximum yield (8.5% C) is observed on MFI-MTW/ Al_2O_3 . In terms of catalyst micropore volume, the samples are in the inverse sequence MFI-MTW/ $\text{Al}_2\text{O}_3 < \text{MFI-MCM-41}/\text{Al}_2\text{O}_3 < \text{MFI-MEL}/\text{Al}_2\text{O}_3$: $0.012 < 0.040 < 0.088 \text{ cm}^3/\text{g}(\text{cat})$.

The greater the number of micropores, the greater the number of diffusion restrictions. In the case of successive reactions, diffusion restrictions lead to a longer contact of intermediate products with the inner surface of the catalyst, which leads to more active secondary reactions. Methanol is an intermediate product. The priority pathway for its formation is the methylation of olefins and aromatics by DME [25,45]. Subsequently, methanol itself reacts as a methylating agent and is consumed. Therefore, the dependence of the methanol yield on the specified contact time passes through a maximum, then decreases. When methanol is formed in the system, it competes with DME in the diffusion rate into zeolite micropores and the participation in methylation reactions. The more micropores in the catalyst, the greater the methanol participation in methylation reactions due to smaller molecular size. That leads to the lower methanol yield observed in the gas phase.

The hypothesis about the determining role of micropores in the hydrocarbon pool formation and in the rate of products diffusion is supported by the graphical dependences of the products distribution (% mol) on DME conversion (Figure 4). In Figure 4, product selectivities are located one above the other along the Y-axis, and their sum is 100%. The product composition at a specified DME conversion is determined by the width of the bands corresponding to a specific component. For example, for a standard MFI/ Al_2O_3 catalyst at a DME conversion of 43%, the selectivity for the formation of ethylene, propylene, butenes, and methanol is 9.3, 17.9, 7.7, and 48.5% mol, respectively.

The hybrid zeolite-based MFI-MEL/ Al_2O_3 catalyst is characterized by the highest ethylene and propylene selectivity over the entire DME conversion range among the studied samples. The selectivity for ethylene and propylene is 19.4 and 24.2% mol at 50% DME conversion, and 26.8 and 22.2% mol at 95% DME conversion (Figure 4A), respectively. The ratio of ethylene/propylene ranges from 0.7 to 1.2 (Figure 5).

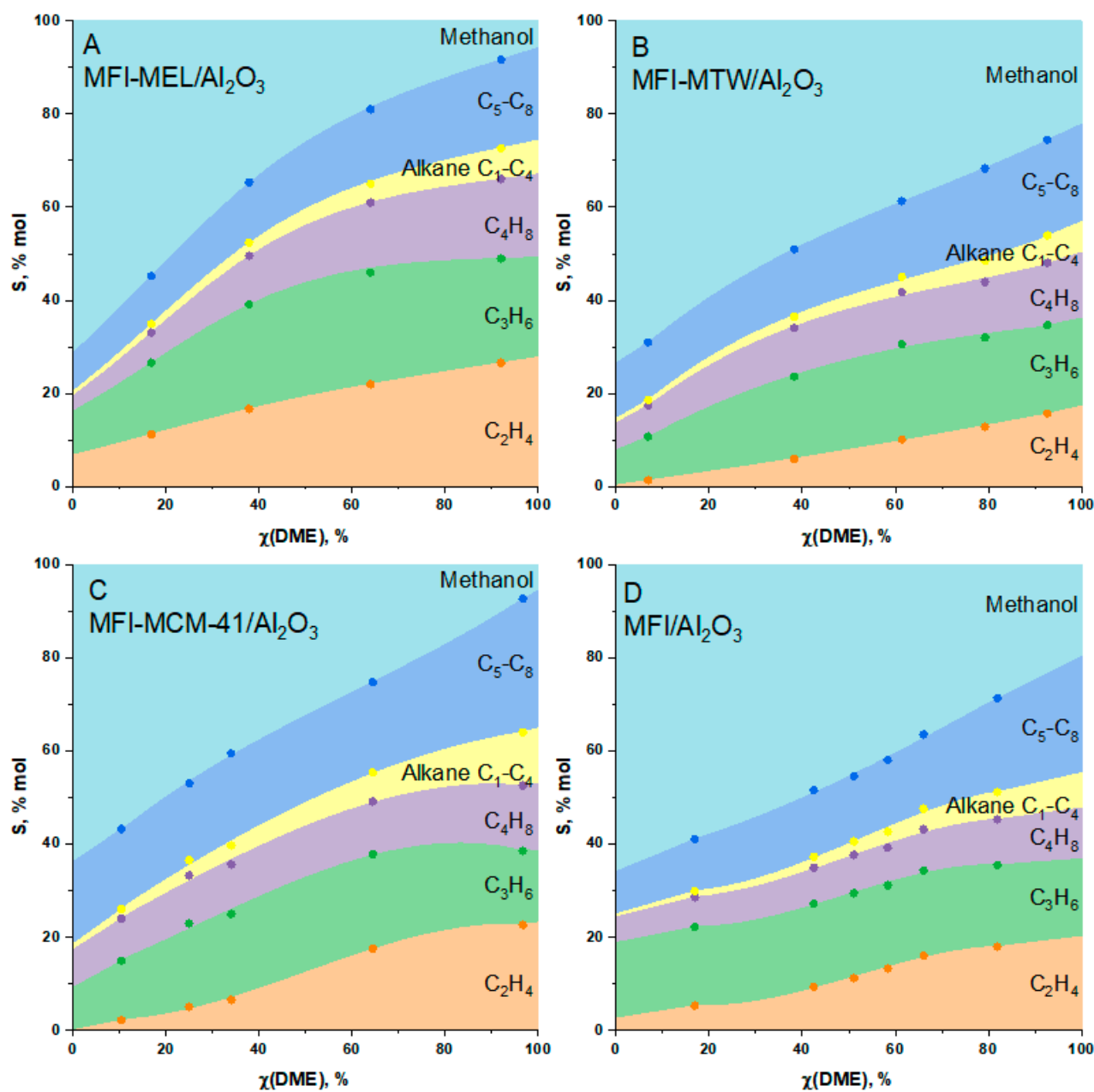


Figure 4. Dependence of the product selectivity (C₂-C₄ olefins, C₁-C₄ alkanes, C₅-C₈ hydrocarbons, and methanol) on DME conversion on catalysts (A) MFI-MEL/Al₂O₃, (B) MFI-MTW/Al₂O₃, (C) MFI-MCM-41/Al₂O₃, (D) MFI/Al₂O₃. *p* = 1 atm, *T* = 340 °C.

On the catalyst based on hybrid zeolite MFI-MTW/Al₂O₃, the selectivity for ethylene and propylene is 8.3 and 19.4% at 50% DME conversion and 16.4 and 18.8% at 95% DME conversion, respectively. In the range of low DME conversion values, the selectivity of ethylene is close to zero (Figure 4B). The ethylene/propylene ratio ranges from 0.15 to 0.75 (Figure 5).

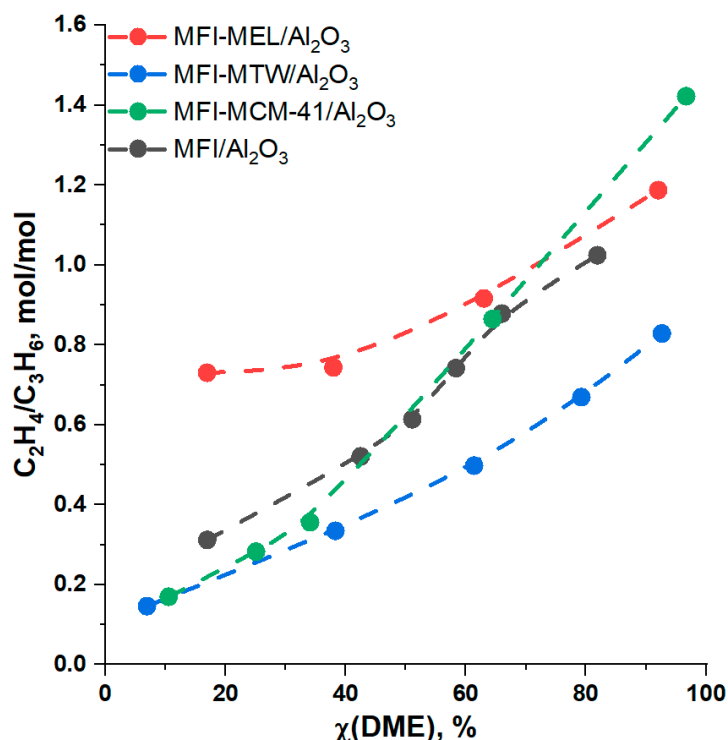


Figure 5. Ethylene/Propylene mole ratio as a function of DME conversion. $p = 1$ atm, $T = 340$ °C.

The MFI-MCM-41/Al₂O₃ catalyst is characterized by the product distribution, which can be defined as “average” between the two samples MFI-MEL/Al₂O₃ and MFI/Al₂O₃. Like MFI-MEL/Al₂O₃, it has a high ethylene and propylene selectivity—12.5 and 20.5% at 50% DME conversion, and 23.0 and 16.4% at 95% DME conversion (Figure 4C), respectively. At the same time, the selectivities of C₅–C₈ hydrocarbons and C₁–C₄ alkanes on the MFI-MCM-41/Al₂O₃ are the highest: up to 30% mol. and up to 12% mol, respectively. An additional feature of this catalyst is a sharp increase in the ethylene/propylene ratio from 0.18 to 1.4 with an increase in DME conversion. The ratio increases due to an increase in the ethylene selectivity from 1.7 to 12.3% mol, while the propylene selectivity remains approximately constant at 15–20% mol over the entire range of DME conversions (Figure 5).

As mentioned above, the MFI-MEL/Al₂O₃ catalyst has the highest micropore volume and the highest ethylene/propylene ratio. On the other hand, the MFI-MTW/Al₂O₃ catalyst has almost no micropores and has the lowest ethylene/propylene ratio.

The increase in the yield of ethylene on MFI-MEL/Al₂O₃ can be related to the low rate of diffusion of C₅–C₈ hydrocarbons from zeolite micropores. According to the dual-cycle mechanism, aromatic polymethyl-substituted intermediates are formed from C₅–C₈ hydrocarbons. Methylation and dealkylation of this type of hydrocarbon pool species lead to the formation of ethylene [12,23,67]. Thus, diffusion difficulties of C₅–C₈ hydrocarbons in zeolite micropores determine the yield of ethylene.

In addition to hydrocarbon selectivity, isomerizing activity and activity in hydrogen transfer reactions are important characteristics for zeolite catalysts.

The comparison of the hydrogen transfer index in C₂–C₅ hydrocarbons for the studied samples is shown in Figure 6. The hydrogen transfer index HTI is calculated according to the standard method as the ratio of the number of alkanes with n carbon atoms to the total number of alkanes and alkenes with n carbon atoms [68,69].

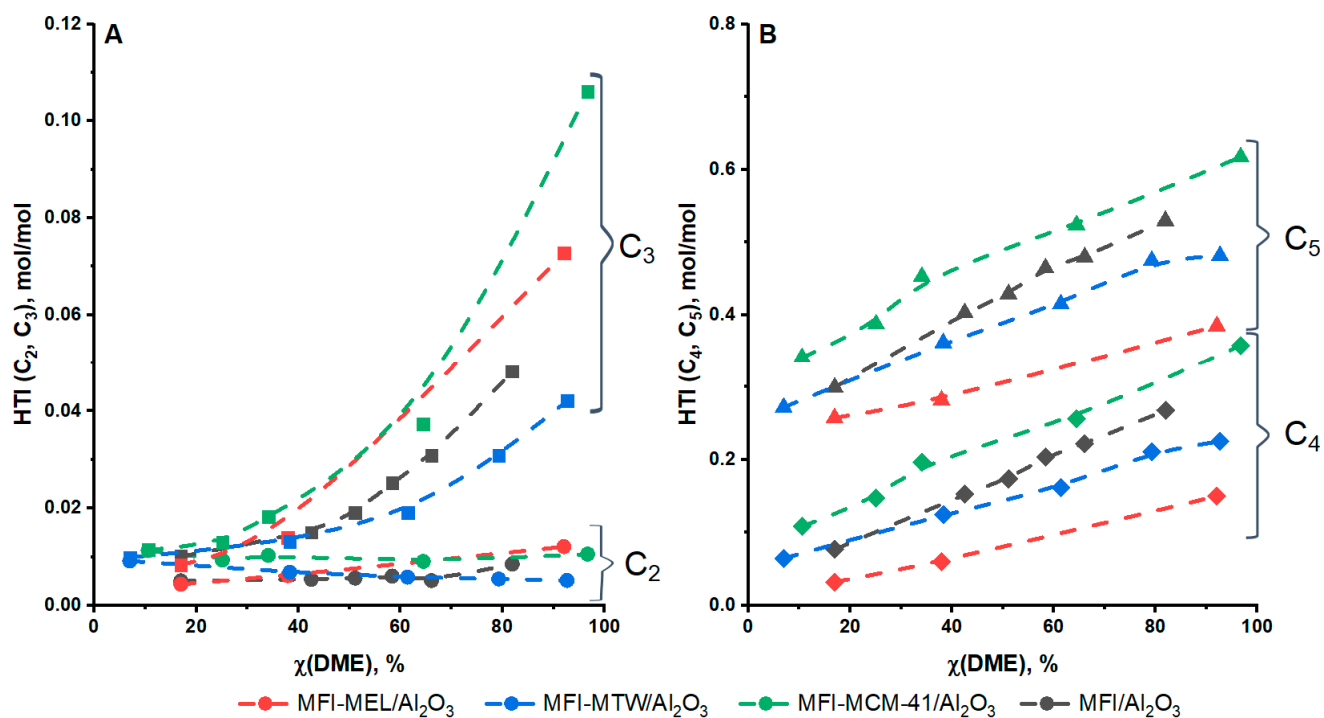


Figure 6. Hydrogen transfer index (HTI) for hydrocarbons with chain length (A) 2 (●), 3 (■), (B) 4 (◆), and 5 (▲) for MF-MEL/Al₂O₃, MFI-MTW/Al₂O₃, MFI-MCM-41/Al₂O₃, MFI/Al₂O₃ catalysts, respectively. $p = 1$ atm, $T = 340$ °C.

The hydrogen transfer index increases in the series $C_2 < C_3 < C_4 < C_5$ as shown in Figure 6. The HT-index for C_2 hydrocarbons is low (less than 0.012), and it almost does not depend on the DME conversion for all studied samples. The dependence of the HT-index for C_3 hydrocarbons on DME conversion can be approximated by an exponential function and for C_4 – C_5 hydrocarbons by a linear one. This means that for C_3 – C_5 hydrocarbons, the rate of the H-transfer reaction increases with an increase in DME conversion. Consequently, the contribution of hydrogen transfer reactions to the distribution of products also increases—the yield of alkanes rises.

In comparison to other samples, the MFI-MEL/Al₂O₃ is characterized by a high HT-index for C_3 hydrocarbons (0.075 at a DME conversion of 95%) and minimum HT-index for C_4 and C_5 hydrocarbons (0.15 and 0.38 at a DME conversion of 95%).

The maximum HT-index for C_3 – C_5 hydrocarbons is observed for MFI-MCM-41/Al₂O₃. This catalyst has a large mesopore volume (0.300 cm³/g) and it is not a catalyst with a low activity as MFI-MTW/Al₂O₃ is. As the hydrogen transfer reaction proceeds between the lower and higher olefins, the coordination of the reactants requires space, which is apparently provided by the mesopores of the hybrid structure.

To estimate the isomerizing activity of the catalysts, the dependences of the iso-/n-alkenes mole ratio on DME conversion were plotted (Figure 7).

It can be seen that the ratio of iso-/n-isomers does not depend on the DME conversion, and all the studied samples have the same isomerizing activity. Olefins with a longer carbon chain are more actively involved in isomerization: the iso-/n-ratio for C_4H_8 olefins is 0.08, and for C_5H_{10} olefins, it is 0.38.

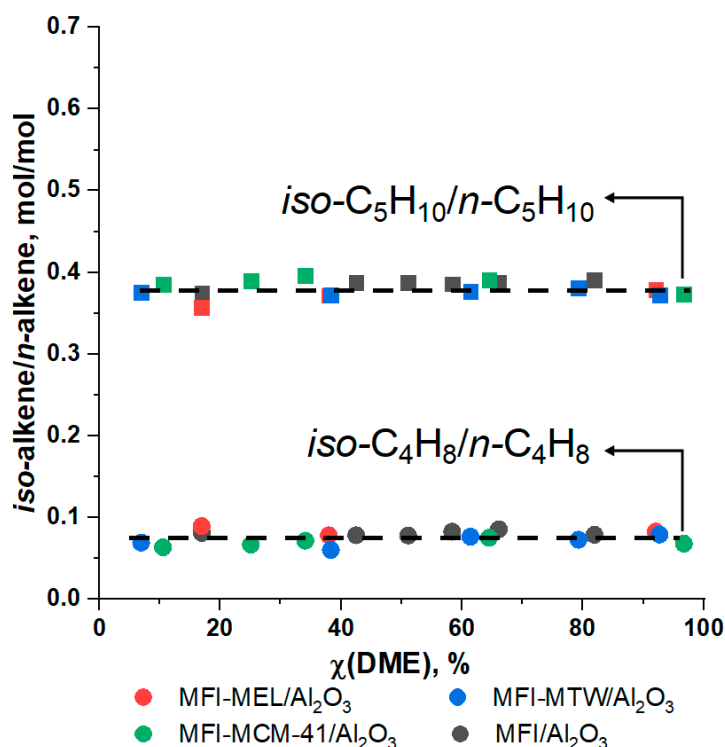


Figure 7. Iso-/n-olefins mole ratio as a function of DME conversion for MF-MEL/Al₂O₃, MFI-MTW/Al₂O₃, MFI-MCM-41/Al₂O₃, MFI/Al₂O₃ catalysts. $p = 1$ atm, $T = 340$ °C.

3. Materials and Methods

3.1. Catalyst Synthesis

Hybrid zeolites MFI-MEL, MFI-MTW, and MFI-MCM-41 were synthesized according to the method described in patents [50,70].

The industrial zeolite IK-17-1 (Novosibirsk Chemical Concentrates Plant (NCCP), Novosibirsk, Russia) was used as the MFI zeolite, which is the Russian analog of the ZSM-5 zeolite (Zeolyst, Conshohocken, PA, USA).

3.1.1. MFI-MEL Synthesis

Amounts of 3.73 g of aluminum decahydrate sulfate and 10.1 g of N^1, N^{10} -bis(2-hydroxyethyl)- N^1, N^1, N^{10}, N^{10} -tetramethyldecane-1,10-diammonium bromide are dissolved in 12.6 g of distilled water (Solution 1).

Then, with stirring, 1.5 g of sodium hydroxide was added to Solution 1—the solution was stirred until the solid reagents were dissolved (Solution 2).

In a separate container, 25.2 g of a 40% (wt.) colloidal solution of silicon dioxide brand LUDOX HS-40 and 10.1 g of water were mixed until homogeneous (Solution 3).

Solution 2 was added dropwise to Solution 3 and mixed until a homogeneous gel-like mass was formed. For crystallization, the resulting gel was placed in a Teflon cup of the autoclave, sealed, and thermostated at 160 °C for 3 days. The resulting product was filtered off under reduced pressure (101.325 kPa) on a glass porous filter and washed with distilled water until the pH of the filtrate reached 9.0. The sample was transferred to a Petri dish and dried in an oven at 100 °C for 12 h; calcined in a muffle furnace, starting from room temperature, then with a heating step of 1 °C/min up to 520 °C, then at this temperature for 6 h. Ion exchange to obtain the NH₄ form of the zeolite was carried out with a 1.1 M aqueous solution of ammonium chloride for 15 h. The mixture was filtered under reduced pressure (98.5 kPa) on a porous glass filter, washed with distilled water until the pH of the filtrate reached 8.0, and dried in an oven at 100 °C for 12 h; calcined in a muffle furnace,

starting from room temperature, then with a heating step of 1 °C/min up to 460 °C, then at this temperature for 4 h to obtain the H-form of the zeolite.

3.1.2. MFI-MTW Synthesis

Hybrid-structure zeolite MFI-MTW was prepared similarly to MFI-MEL with the difference that Solution 1 was prepared as follows: 3.73 g of aluminum decahydrate sulfate and 10.1 g of 8.95 g of *N*¹,*N*⁶-bis(2) bromide-hydroxyethyl)-*N*¹,*N*¹,*N*⁶,*N*⁶-tetramethylhexane-1,6-diammonium were dissolved in 12.6 g of distilled water.

3.1.3. MFI-MCM-41 Synthesis

Amounts of 0.69 g of sodium hydroxide, 5.8 mL of a 1 M solution of tetrapropylammonium hydroxide, and 35.5 mL of water were stirred until all components were completely dissolved. An amount of 6.9 g of pyrogenic silicon dioxide was added to the resulting solution for an hour in portions with continued stirring, and the mixture was stirred at room temperature for another 1 h; then, the mixture was placed in a Teflon cup (Solution 1).

In a separate Teflon cup, 2.20 g of hexadecyltrimethylammonium bromide, 0.44 g of sodium hydroxide, and 43.3 mL of water were mixed until complete dissolution of the template. An amount of 0.51 g of sodium aluminate was added to the resulting solution and mixed. An amount of 4.92 g of silicon dioxide was added to the resulting solution in portions with stirring for one hour. The mixture was stirred for three hours at room temperature until complete homogenization (Solution 2).

Both Solution 1 and Solution 2 were placed in an autoclave and thermostated at 100 °C for 16 h. An amount of 6 g of Solution 1 was added to Solution 2 in a Teflon cup. The resulting mixture was stirred on a mechanical stirrer until homogeneous for one hour. For crystallization, the resulting mixture was placed in the autoclave, sealed, and thermostated at 180 °C for 3 days. The resulting product was filtered off under reduced pressure (101.3 kPa) on a glass porous filter and washed with distilled water until the pH of the filtrate reached 9.0. The sample was transferred to a Petri dish and dried in an oven at 90 °C for 6 h; calcined in a muffle furnace, starting from room temperature, then with a heating step of 1 °C/min up to 550 °C, then at this temperature for 6 h. Ion exchange to obtain the NH₄ form of the zeolite was carried out with a 1.1 M aqueous solution of ammonium chloride at 85 °C for 2 h. The mixture was filtered under reduced pressure (98.5 kPa) on a porous glass filter, washed with distilled water until the pH of the filtrate reached 8.0, and dried in an oven at 90 °C for 6 h; calcined in a muffle furnace, starting from room temperature, then with a heating step of 1 °C/min up to 550 °C, then at this temperature for 5 h to obtain the H-form of the zeolite.

3.1.4. Catalyst Preparation

An amount of 42.7 g of AlO(OH) was placed in a mixer and 20 mL of a peptizing solution (5 mL of 1.0 M aqueous HNO₃ + 15 mL of H₂O) was added. The mixture was stirred for 5 min. An amount of 76.5 g of dry zeolite was added. The mass was stirred for 20 min at 60 °C. After that, the catalytic mass was passed through an extruder with a die diameter of 2.5 mm. The extrudates were dried in an oven at 80 °C, 90 °C, 100 °C, 110 °C, and 120 °C for 3 h at each temperature, then calcined in a muffle furnace at 550 °C for 7 h. During calcination, AlO(OH) was converted to Al₂O₃. The final content of Al₂O₃ in the material obtained was 30% wt.

3.1.5. Hydrothermal Treatment

The MFI/Al₂O₃ standard sample was hydrothermally treated before catalytic experiments at 500 °C for 6 h at WHSV of steam 12 h⁻¹. The detailed description of the catalyst preparation method can be found in the patents [45,71,72].

3.2. Catalyst Characterization

X-ray powder diffraction (XRD) patterns of samples were recorded on a Rigaku Rotaflex RU-200 diffractometer with Cu K α radiation (1.5418 Å, 50 kV, and 160 mA). The zeolites phase ratio was determined by the Reference Intensity Ratio (RIR) method using the MDI Jade 6 program [73].

The textural characteristics of the catalyst samples were studied by N₂ adsorption/desorption isotherms at −196 °C on a Belsorp mini X instrument (MICROTRAC MRB, Osaka, Japan). Prior to measurement, catalyst samples were degassed under a high vacuum at 350 °C and 1.36 10^{−6} atm for 3–6 h. The total specific surface area of the catalyst was determined by the BET method (Brunauer–Emmett–Teller). The total pore volume was determined according to the amount of adsorbed nitrogen at a relative pressure of $p/p_0 = 0.95$. The mesopore volume was determined as the difference between total pore volume and the micropore volume (t-plot). The micropore surface area was calculated as the difference of the total surface area (BET) and sum of the external surface area (t-plot) and the mesopore area (BJH method (Barrett–Joyner–Halenda), desorption curve). The average mesopore diameter was determined by the BJH method and the average micropore diameter was determined by the MP-plot.

The amount, strength, and distribution of acid sites were determined by NH₃-TPD on a chemical adsorption analyzer USGA (Moscow, Russia) with a thermal conductivity detector. All samples (0.15 g) before measurements were pretreated by heating in a helium flow at 500 °C (heating rate of 20 °C/min), calcination at 500 °C for 1 h, and cooling to 60 °C. Then, the samples were saturated with NH₃ for 15 min, flushed with helium at 100 °C for 1 h to remove physically adsorbed NH₃, and cooled to 60 °C. The final desorption of NH₃ was performed at 60–750 °C at a heating rate of 8 °C/min in a helium flow. The released ammonia was recorded using a thermal conductivity detector.

X-ray fluorescence elemental (XRF) analysis was conducted with the Thermo ARL Perform^x Sequential XFR instrument (Thermo Fisher Scientific, Waltham, MA, USA) using a 2500 W X-ray tube. Before the analysis, the samples weighing 200 mg were pressed into a tablet with boric acid.

Scanning electron microscopy (SEM). The micrographs of the samples were taken on a Hitachi (Chiyoda City, Tokyo, Japan) TM3030 desktop scanning electron microscope.

The structure and surface morphology of the synthesized samples were studied using transmission electron microscopy (TEM) on an LEO AB OMEGA instrument with the magnification from 80 to 500,000 and the image resolution of 0.2–0.34 nm.

Nuclear magnetic resonance spectra were recorded at a rotation magnetic angle on a Bruker AVANCE-II 400 WB spectrometer with a magnetic field of 9.4 T, which corresponds to operating frequencies of $\nu(^1\text{H}) = 400.13$ MHz and $\nu(^{27}\text{Al}) = 104.2$ MHz, using a MAS (magic-angle spinning), with the diameter of the MAS-rotor of 4 mm and the rotation frequency of 12,000 Hz. Before registration, air-dry samples were kept in a desiccator with a 25% aqueous ammonia solution for 24 h at room temperature. Spectra on ²⁷Al nuclei were recorded using a single-pulse technique (15° pulse) with the following parameters: the exciting 15° pulse width was 0.8 μs , the number of scans was 1024, and the interval between scans was 0.5 s. An 1 M Al(NO₃)₃·H₂O aqueous solution was utilized as an external reference (0 ppm).

The concentration of acid sites in the samples was determined by the IR spectroscopy of adsorbed pyridine. IR spectra were recorded on a Nicolet Protégé 460 instrument with an optical resolution of 4 cm^{−1} and a range of 4000–400 cm^{−1}. Samples in the form of disks (diameter 1.6 cm, density ~10 mg cm^{−2}) were activated in an IR cell at 400 °C (heating rate of 7.5 deg min^{−1}) for 2 h at a pressure of 10^{−5} Torr. The adsorption of probe molecules was carried out at 150 °C and a pressure of 2 Torr of pyridine for 30 min. At the end of the adsorption cycle, pyridine was desorbed at 150 °C for 15 min. The concentrations of Bronsted acid sites (BAS) and Lewis acid sites (LAS) were determined from the intensity of the adsorbed pyridine bands (1545 and 1450 cm^{−1}, respectively); the molar extinction coefficients were $\epsilon(\text{BAS}) = 1.67$ cm· μmol^{-1} and $\epsilon(\text{LAS}) = 2.22$ cm· μmol^{-1} .

3.3. Catalytic Tests

Catalytic experiments were performed in a fixed-bed continuous flow quartz reactor with an inner diameter of 10 mm at 1 atm and 340 °C. Here, the catalyst, weighing 0.5 g ($d_p = 0.4\text{--}0.63$ mm), was mixed with quartz ($d_p = 0.5\text{--}1.0$ mm) with the volume ratio of 1:1. Prior to the experiment, the catalyst was preheated and purged with nitrogen flow at 400 °C for 1 h to remove physically adsorbed water. The dimethyl ether/nitrogen mixture with a concentration of DME of 10–13% vol was used as a feedstock. The GHSV was varied in the range of 2500–25,000 h⁻¹.

The specified contact time per carbon for DME (τ) varied from 0.2–3.0 g(cat)/g(C)·h, corresponding to DME conversion in the range of 5–95%. The results averaged over three parallel measurements with a relative error of 5–7% were used for the calculation of catalytic activity.

The reaction products were analyzed using an on-line gas chromatograph (Crystallux-4000 M) equipped with a flame ionization detector (FID) and a thermal conductivity detector (TCD). The capillary column with the CP-Poraplot Q phase (27.5 m × 0.32 mm × 10 μm) was used to determine the composition of hydrocarbons C₁–C₈, methanol, and DME. The packed column with a Porapak Q phase (3.0 m × 4 mm × 3 μm) was used to determine N₂. The analysis was performed at the programmed temperature increase from 90 to 250 °C with a heating rate of 30 °C/min, and the carrier gas was helium. Chromatograms were processed using the NetChromWin software (Version 2.0, JSC Scientific Production Company Meta-Chrome, Yoshkar-Ola, Russia, 2017) and hardware systems.

The reaction products observed were methanol, alkenes C₂–C₄, alkanes C₁–C₄, and hydrocarbons C₅–C₈ (alkanes, cyclo-, and aromatic compounds).

The DME conversion (1) and the selectivity of products (2) were used as the main indicators for characterizing the processes. The specified contact time was calculated by Equation (3)

$$\chi_{\text{DME}} = \frac{n_{\text{in}}(\text{DME}) - n_{\text{out}}(\text{DME})}{n_{\text{in}}(\text{DME})}, \% \quad (1)$$

$$S_i = \frac{n_{\text{Ci}}}{\sum_i n_{\text{Ci}}}, \% \text{ mol.} \quad (2)$$

$$\tau = \frac{m_{\text{cat}}}{m_{\text{in,C}}(\text{DME})}, \frac{\text{g}_{\text{cat}} \times \text{h}}{\text{g}_{\text{C}}} \quad (3)$$

where $n_{\text{in}}(\text{DME})$ and $n_{\text{out}}(\text{DME})$ are moles of DME at the reactor inlet and outlet, respectively, n_{Ci} is mole of the i -th carbon-containing compound in products at the reactor outlet, mole; $\sum_i n_{\text{Ci}}$ is the sum of moles of all products at the reactor outlet, mole; m_{cat} is mass of the catalyst, g; $m_{\text{in,C}}(\text{DME})$ is mass flow of carbon in the DME at the reactor inlet, g_C/h.

4. Conclusions

The catalysts based on hybrid zeolites MFI-MEL, MFI-MTW, and MFI-MCM-41 have been studied in the reaction of lower olefins synthesis from dimethyl ether. The texture-acid properties of the samples have been studied, and their influence on the activity and distribution of the reaction products has been established.

It has been shown that the activity of the zeolite catalyst is determined by the total acidity of weak (ammonia desorption temperature $T = 170\text{--}230$ °C) and strong ($T = 350\text{--}380$ °C) active sites, while the participation of medium-strength acid sites ($T = 290$ °C) in the reaction of hydrocarbon formation from oxygenates is unlikely.

It has been shown that the volume of micropores in the catalyst is responsible for the ethylene selectivity and the ethylene/propylene ratio in the reaction products. An increase in the volume of micropores contributes to an increase in the ethylene selectivity due to the stabilization of aromatic hydrocarbon pool species.

It has been shown that the topology of the hybrid zeolite affects the rate of hydrogen transfer reactions but does not affect the isomerizing activity of the catalyst.

Supplementary Materials: The following supporting information can be downloaded at: <https://www.mdpi.com/article/10.3390/catal13030570/s1>, Table S1: Composition of hybrid zeolites; Figure S1: ²⁷Al MAS NMR spectra of hybrid zeolites; Figure S2: IR spectra of pyridine adsorbed on hybrid zeolites; Table S2: Acid characteristics of hybrid zeolites; Figure S3: The micrographs of SEM- and TEM-hybrid zeolite; Table S3: Additional textural properties of the catalysts, Figure S4: BJH plots (desorption curve) for the catalysts, Figure S5: t-Plots for nitrogen adsorbed in the catalysts.

Author Contributions: Conceptualization, M.V.M. and A.V.S.; methodology, I.A.D. and D.E.T.; formal analysis, A.V.S.; resources, A.L.M.; writing—original draft preparation, A.V.S.; writing—review and editing, M.V.M.; visualization, A.V.S.; supervision, M.V.M.; project administration, A.L.M. All authors have read and agreed to the published version of the manuscript.

Funding: This work was financially supported by the Russian Science Foundation (grant No. 17-73-30046).

Data Availability Statement: The data presented in this study are available on request from the corresponding author.

Acknowledgments: The authors are grateful to Andrey Smirnov (M.V. Lomonosov Moscow State University), Vladislav Malyavin (A.V. Topchiev Institute of Petrochemical Synthesis, RAS), Ivan Levin (A.V. Topchiev Institute of Petrochemical Synthesis, RAS), and Sergey Sorokin (A.V. Topchiev Institute of Petrochemical Synthesis, RAS) for their help in physicochemical studies of catalysts and interpretation of the results. The authors are thankful to Svetlana Bychkova for her help in English editing.

Conflicts of Interest: The authors declare no conflict of interest.

References

1. Tian, P.; Wei, Y.; Ye, M.; Liu, Z. Methanol to olefins (MTO): From fundamentals to commercialization. *ACS Catal.* **2015**, *5*, 1922–1938. [[CrossRef](#)]
2. Yang, M.; Fan, D.; Wei, Y.; Tian, P.; Liu, Z. Recent Progress in Methanol-to-Olefins (MTO) Catalysts. *Adv. Mater.* **2019**, *31*, 1902181. [[CrossRef](#)]
3. Chang, C.D.; Silvestri, A.J.; Smith, R.L. (MTG) Production of Gasoline Hydrocarbons. U.S. Patent 3,928,483, 23 December 1975.
4. Chang, C.D.; Lang, W.H. Process for Manufacturing Olefins. U.S. Patent 566,166, 24 May 1977.
5. Li, J.; Wei, Z.; Chen, Y.; Jing, B.; He, Y.; Dong, M.; Jiao, H.; Li, X.; Qin, Z.; Wang, J.; et al. A route to form initial hydrocarbon pool species in methanol conversion to olefins over zeolites. *J. Catal.* **2014**, *317*, 277–283. [[CrossRef](#)]
6. Yarulina, I.; Chowdhury, A.D.; Meirer, F.; Weckhuysen, B.M.; Gascon, J. Recent trends and fundamental insights in the methanol-to-hydrocarbons process. *Nat. Catal.* **2018**, *1*, 398–411. [[CrossRef](#)]
7. Liu, Y.; Müller, S.; Berger, D.; Jelic, J.; Reuter, K.; Tonigold, M.; Sanchez-Sanchez, M.; Lercher, J.A. Formation mechanism of the first carbon–carbon bond and the first olefin in the methanol conversion into hydrocarbons. *Angew. Chem. Int. Ed.* **2016**, *55*, 5723–5726. [[CrossRef](#)]
8. Wu, X.; Xu, S.; Zhang, W.; Huang, J.; Li, J.; Yu, B.; Wei, Y.; Liu, Z. Direct mechanism of the first carbon–carbon bond formation in the methanol-to-hydrocarbons process. *Angew. Chem. Int. Ed.* **2017**, *56*, 9039–9043. [[CrossRef](#)]
9. Salehirad, F.; Anderson, M.W. Solid-state ¹³C MAS NMR study of methanol-to-hydrocarbon chemistry over H-SAPO-34. *J. Catal.* **1996**, *164*, 301–314. [[CrossRef](#)]
10. Ivanova, I.I.; Pomakhina, E.B.; Rebrov, A.I.; Hunger, M.; Kolyagin, Y.G.; Weitkamp, J. Surface species formed during aniline methylation on zeolite H-Y investigated by in situ MAS NMR spectroscopy. *J. Catal.* **2001**, *203*, 375–381. [[CrossRef](#)]
11. Van Der Mynsbrugge, J.; Moors, S.L.C.; De Wispelaere, K.; Van Speybroeck, V. Insight into the formation and reactivity of framework-bound methoxide species in h-zsm-5 from static and dynamic molecular simulations. *ChemCatChem* **2014**, *6*, 1906–1918. [[CrossRef](#)]
12. Svelle, S.; Joensen, F.; Nerlov, J.; Olsbye, U.; Lillerud, K.P.; Kolboe, S.; Bjørgen, M. Conversion of methanol into hydrocarbons over zeolite H-ZSM-5: Ethene formation is mechanistically separated from the formation of higher alkenes. *J. Am. Chem. Soc.* **2006**, *128*, 14770–14771. [[CrossRef](#)] [[PubMed](#)]
13. Bjørgen, M.; Svelle, S.; Joensen, F.; Nerlov, J.; Kolboe, S.; Bonino, F.; Palumbo, L.; Bordiga, S.; Olsbye, U. Conversion of methanol to hydrocarbons over zeolite H-ZSM-5: On the origin of the olefinic species. *J. Catal.* **2007**, *249*, 195–207. [[CrossRef](#)]
14. Bjørgen, M.; Lillerud, K.P.; Olsbye, U.; Svelle, S. Conversion of methanol to hydrocarbons: Hints to rational catalyst design from fundamental mechanistic studies on H-ZSM-5. *Stud. Surf. Sci. Catal.* **2007**, *167*, 463–468. [[CrossRef](#)]
15. Olsbye, U.; Svelle, S.; Bjørgen, M.; Beato, P.; Janssens, T.V.W.; Joensen, F.; Bordiga, S.; Lillerud, K.P. Conversion of methanol to hydrocarbons: How zeolite cavity and pore size controls product selectivity. *Angew. Chem. Int. Ed.* **2012**, *51*, 5810–5831. [[CrossRef](#)]
16. Lu, C.; Yang, H.; Wang, J.; Tan, Q.; Fu, L. Utilization of iron tailings to prepare high-surface area mesoporous silica materials. *Sci. Total Environ.* **2020**, *736*, 139483. [[CrossRef](#)]
17. Hunger, M.; Horvath, T. Adsorption of methanol on Bronsted acid sites in zeolite H-ZSM-5 investigated by multinuclear solid-state NMR spectroscopy. *J. Am. Chem. Soc.* **1996**, *118*, 12302–12308. [[CrossRef](#)]

18. Seiler, M.; Schenk, U.; Hunger, M. Conversion of methanol to hydrocarbons on zeolite HZSM-5 investigated by in situ MAS NMR spectroscopy under flow conditions and on-line gas chromatography. *Catal. Lett.* **1999**, *62*, 139–145. [[CrossRef](#)]
19. Seiler, M.; Wang, W.; Hunger, M. Local structure of framework aluminum in zeolite H-ZSM-5 during conversion of methanol investigated by in situ NMR spectroscopy. *J. Phys. Chem. B* **2001**, *105*, 8143–8148. [[CrossRef](#)]
20. Hunger, M.; Seiler, M.; Buchholz, A. In situ MAS NMR spectroscopic investigation of the conversion of methanol to olefins on silicoaluminophosphates SAPO-34 and SAPO-18 under continuous flow conditions. *Catal. Lett.* **2001**, *74*, 61–68. [[CrossRef](#)]
21. Wang, W.; Seiler, M.; Hunger, M. Role of surface methoxy species in the conversion of methanol to dimethyl ether on acidic zeolites investigated by in situ stopped-flow MAS NMR spectroscopy. *J. Phys. Chem. B* **2001**, *105*, 12553–12558. [[CrossRef](#)]
22. Wang, C.; Sun, X.; Xu, J.; Qi, G.; Wang, W.; Zhao, X.; Li, W.; Wang, Q.; Deng, F. Impact of temporal and spatial distribution of hydrocarbon pool on methanol conversion over H-ZSM-5. *J. Catal.* **2017**, *354*, 138–151. [[CrossRef](#)]
23. Yarulina, I.; De Wispelaere, K.; Bailleul, S.; Goetze, J.; Radersma, M.; Abou-Hamad, E.; Vollmer, I.; Goesten, M.; Mezari, B.; Hensen, E.J.M.; et al. Structure–performance descriptors and the role of Lewis acidity in the methanol-to-propylene process. *Nat. Chem.* **2018**, *10*, 804–812. [[CrossRef](#)]
24. Liu, C.; Uslamin, E.A.; Pidko, E.A.; Kapteijn, F. Direct discerning reaction pathways in methanol-to-hydrocarbons by transient operation–FASPA. *Chem. Eng. J.* **2023**, *453*, 139696. [[CrossRef](#)]
25. Magomedova, M.; Starozhitskaya, A.; Davidov, I.; Maximov, A.; Kravtsov, M. Dual-cycle mechanism based kinetic model for dme-to-olefin synthesis on hzsm-5-type catalysts. *Catalysts* **2021**, *11*, 1459. [[CrossRef](#)]
26. Dahl, I.M.; Kolboe, S. On the reaction mechanism for hydrocarbon formation from methanol over SAPO-34. I. Isotopic labeling studies of the co-reaction of ethene and methanol. *J. Catal.* **1994**, *149*, 458–464. [[CrossRef](#)]
27. Xiao, J.; Wei, J. Diffusion of Hydrocarbons Theory. *Chem. Eng. Sci.* **1992**, *47*, 1123–1141. [[CrossRef](#)]
28. Xiao, J.; Wei, J. Diffusion mechanism of hydrocarbons in zeolites-II. Analysis of experimental observations. *Chem. Eng. Sci.* **1992**, *47*, 1143–1159. [[CrossRef](#)]
29. Sharbini Kamaluddin, H.; Gong, X.; Ma, P.; Narasimharao, K.; Dutta Chowdhury, A.; Mokhtar, M. Influence of zeolite ZSM-5 synthesis protocols and physicochemical properties in the methanol-to-olefin process. *Mater. Today Chem.* **2022**, *26*, 101061. [[CrossRef](#)]
30. Weissenberger, T.; Machoke, A.G.F.; Bauer, J.; Dotzel, R.; Casci, J.L.; Hartmann, M.; Schwieger, W. Hierarchical ZSM-5 Catalysts: The Effect of Different Intracrystalline Pore Dimensions on Catalyst Deactivation Behaviour in the MTO Reaction. *ChemCatChem* **2020**, *12*, 2461–2468. [[CrossRef](#)]
31. Bai, R.; Song, Y.; Li, Y.; Yu, J. Creating Hierarchical Pores in Zeolite Catalysts. *Trends Chem.* **2019**, *1*, 601–611. [[CrossRef](#)]
32. Chen, L.H.; Sun, M.H.; Wang, Z.; Yang, W.; Xie, Z.; Su, B.L. Hierarchically structured zeolites: From design to application. *Chem. Rev.* **2020**, *120*, 11194–11294. [[CrossRef](#)] [[PubMed](#)]
33. Weckhuysen, B.M.; Fu, D.; Maris, J.J.E.; Stanciakova, K. Unravelling Channel Structure–Diffusivity Relationships in Zeolite ZSM-5 at the Single-Molecule Level. *Angew. Chem. Int. Ed.* **2022**, *61*, e202114388. [[CrossRef](#)]
34. Magomedova, M.V.; Afokin, M.I.; Starozhitskaya, A.V.; Galanova, E.G. Pilot Test of Olefin Synthesis from Dimethyl Ether in a Synthesis Gas Atmosphere. *Ind. Eng. Chem. Res.* **2021**, *60*, 4602–4609. [[CrossRef](#)]
35. Vu, X.H.; Armbruster, U.; Martin, A. Micro/mesoporous zeolitic composites: Recent developments in synthesis and catalytic applications. *Catalysts* **2016**, *6*, 183. [[CrossRef](#)]
36. Ivanova, I.I.; Knyazeva, E.E. Micro-mesoporous materials obtained by zeolite recrystallization: Synthesis, characterization and catalytic applications. *Chem. Soc. Rev.* **2013**, *42*, 3671–3688. [[CrossRef](#)] [[PubMed](#)]
37. Schwieger, W.; Machoke, A.G.; Weissenberger, T.; Inayat, A.; Selvam, T.; Klumpp, M.; Inayat, A. Hierarchy concepts: Classification and preparation strategies for zeolite containing materials with hierarchical porosity. *Chem. Soc. Rev.* **2016**, *45*, 3353–3376. [[CrossRef](#)] [[PubMed](#)]
38. Pérez-Ramírez, J.; Christensen, C.H.; Egeblad, K.; Christensen, C.H.; Groen, J.C. Hierarchical zeolites: Enhanced utilisation of microporous crystals in catalysis by advances in materials design. *Chem. Soc. Rev.* **2008**, *37*, 2530–2542. [[CrossRef](#)]
39. Shoinkhorova, T.; Dikhtiarenko, A.; Ramirez, A.; Dutta Chowdhury, A.; Caglayan, M.; Vittenet, J.; Bendjeriou-Sedjerari, A.; Ali, O.S.; Morales-Osorio, I.; Xu, W.; et al. Shaping of ZSM-5-Based Catalysts via Spray Drying: Effect on Methanol-to-Olefins Performance. *ACS Appl. Mater. Interfaces* **2019**, *11*, 44133–44143. [[CrossRef](#)] [[PubMed](#)]
40. Miao, C.; Shang, K.; Liang, L.; Chen, S.; Ouyang, J. Efficient and Stable Ni/ZSM-5@MCM-41 Catalyst for CO₂ Methanation. *ACS Sustain. Chem. Eng.* **2022**, *10*, 12771–12782. [[CrossRef](#)]
41. Millward, G.R.; Ramdas, S.; Thomas, J.M.; Barlow, M.T. Evidence for semi-regularly ordered sequences of mirror and inversion symmetry planes in ZSM-5/ZSM-11 shape-selective zeolitic catalysts. *J. Chem. Soc. Faraday Trans. 2 Mol. Chem. Phys.* **1983**, *79*, 1075–1082. [[CrossRef](#)]
42. Li, P.; Zhang, W.; Han, X.; Bao, X. Conversion of methanol to hydrocarbons over phosphorus-modified ZSM-5/ZSM-11 intergrowth zeolites. *Catal. Lett.* **2010**, *134*, 124–130. [[CrossRef](#)]
43. Kim, J.J.; Jeong, D.J.; Jung, H.S.; Hur, Y.G.; Choung, J.W.; Baik, J.H.; Park, M.J.; Chung, C.H.; Bae, J.W. Dimethyl ether conversion to hydrocarbons on the closely interconnected FER@ZSM-5 nanostructures. *Microporous Mesoporous Mater.* **2022**, *340*, 112034. [[CrossRef](#)]

44. Liu, C.; Uslamin, E.A.; van Vreeswijk, S.H.; Yarulina, I.; Ganapathy, S.; Weckhuysen, B.M.; Kapteijn, F.; Pidko, E.A. An integrated approach to the key parameters in methanol-to-olefins reaction catalyzed by MFI/MEL zeolite materials. *Chin. J. Catal.* **2022**, *43*, 1879–1893. [[CrossRef](#)]
45. Magomedova, M.; Galanova, E.; Davidov, I.; Afokin, M.; Maximov, A. Dimethyl Ether to Olefins over Modified ZSM-5 Based Catalysts Stabilized by Hydrothermal Treatment. *Catalysts* **2019**, *9*, 485. [[CrossRef](#)]
46. Bin, F.; Song, C.; Lv, G.; Song, J.; Wu, S.; Li, X. Selective catalytic reduction of nitric oxide with ammonia over zirconium-doped copper/ZSM-5 catalysts. *Appl. Catal. B Environ.* **2014**, *150–151*, 532–543. [[CrossRef](#)]
47. Kokotailo, G.T.; Chu, P.; Lawton, S.L.; Meier, W.M. Synthesis and structure of synthetic zeolite ZSM-11. *Nature* **1978**, *275*, 119–120. [[CrossRef](#)]
48. Dugkhuntod, P.; Imyen, T.; Wannapakdee, W.; Yutthalekha, T.; Salakhum, S.; Wattanakit, C. Synthesis of hierarchical ZSM-12 nanolayers for levulinic acid esterification with ethanol to ethyl levulinate. *RSC Adv.* **2019**, *9*, 18087–18097. [[CrossRef](#)]
49. Conte, M.; Xu, B.; Davies, T.E.; Bartley, J.K.; Carley, A.F.; Taylor, S.H.; Khalid, K.; Hutchings, G.J. Enhanced selectivity to propene in the methanol to hydrocarbons reaction by use of ZSM-5/11 intergrowth zeolite. *Microporous Mesoporous Mater.* **2012**, *164*, 207–213. [[CrossRef](#)]
50. Maksimov, A.L.; Magomedova, M.V.; Afokin, M.I.; Tsaplin, D.E.; Kulikov, L.A.; Ionin, D.A. Method for Producing an HZSM-Type Zeolite (Variants) and Method for Producing Aromatic Hydrocarbons of the C6-C11 Fraction. RU Patent 2753263C1, 8 December 2021.
51. Lemus-Yegres, L.J.; Such-Basáñez, I.; Román-Martínez, M.C.; de Lecea, C.S.M. Catalytic properties of a Rh-diamine complex anchored on activated carbon: Effect of different surface oxygen groups. *Appl. Catal. A Gen.* **2007**, *331*, 26–33. [[CrossRef](#)]
52. Wang, Q.; Cui, Z.-M.; Cao, C.-Y.; Song, W.-G. 0.3 Å Makes the Difference: Dramatic Changes in Methanol-to-Olefin Activities between H-ZSM-12 and H-ZSM-22 Zeolites. *J. Phys. Chem. C* **2011**, *115*, 24987–24992. [[CrossRef](#)]
53. Karge, H.G. Comparative Measurements on Acidity of Zeolites. *Stud. Surf. Sci. Catal.* **1991**, *65*, 133–156. [[CrossRef](#)]
54. Lónyi, F.; Valyon, J. On the interpretation of the NH₃-TPD patterns of. *Microporous Mesoporous Mater.* **2001**, *47*, 293–301. [[CrossRef](#)]
55. Serrano, D.P.; García, R.A.; Vicente, G.; Linares, M.; Procházková, D.; Čejka, J. Acidic and catalytic properties of hierarchical zeolites and hybrid ordered mesoporous materials assembled from MFI protozeolitic units. *J. Catal.* **2011**, *279*, 366–380. [[CrossRef](#)]
56. Malinowski, P.J.; Derzsi, M.; Mazej, Z.; Jagličić, Z.; Gawel, B.; Łasocha, W.; Grochala, W. AgIIso₄: A genuine sulfate of divalent silver with anomalously strong one-dimensional antiferromagnetic Interactions. *Angew. Chem. Int. Ed.* **2010**, *49*, 1683–1686. [[CrossRef](#)] [[PubMed](#)]
57. Valyon, J.; Lo, F. A TPD and IR study of the surface species formed from ammonia on zeolite H-ZSM-5, H-mordenite, and H-beta. *Thermochim. Acta* **2001**, *373*, 53–57.
58. Corma, A.; Fornés, V.; Navarro, M.T.; Pérez-Pariente, J. Acidity and stability of MCM-41 crystalline aluminosilicates. *J. Catal.* **1994**, *148*, 569–574. [[CrossRef](#)]
59. Kosslick, H.; Lischke, G.; Parlitz, B.; Storek, W.; Fricke, R. Acidity and active sites of Al-MCM-41. *Appl. Catal. A Gen.* **1999**, *184*, 49–60. [[CrossRef](#)]
60. Jentys, A.; Pham, N.H.; Vinek, H. Nature of hydroxy groups in MCM-41. *J. Chem. Soc. Faraday Trans.* **1996**, *92*, 3287–3291. [[CrossRef](#)]
61. Hunger, M.; Schenk, U.; Breuninger, M.; Gläser, R.; Weitkamp, J. Characterization of the acid sites in MCM-41-type materials by spectroscopic and catalytic techniques. *Microporous Mesoporous Mater.* **1999**, *27*, 261–271. [[CrossRef](#)]
62. Chen, C.-Y.; Li, H.-X.; Davis, M.E. Studies on mesoporous materials. *Microporous Mater.* **1993**, *2*, 17–26. [[CrossRef](#)]
63. Silaghi, M.C.; Chizallet, C.; Raybaud, P. Challenges on molecular aspects of dealumination and desilication of zeolites. *Microporous Mesoporous Mater.* **2014**, *191*, 82–96. [[CrossRef](#)]
64. Pérez-Urriarte, P.; Ateka, A.; Aguayo, A.T.; Gayubo, A.G.; Bilbao, J. Kinetic model for the reaction of DME to olefins over a HZSM-5 zeolite catalyst. *Chem. Eng. J.* **2016**, *302*, 801–810. [[CrossRef](#)]
65. Naik, S.P.; Bui, V.; Ryu, T.; Miller, J.D.; Zmierczak, W. Al-MCM-41 as methanol dehydration catalyst. *Appl. Catal. A Gen.* **2010**, *381*, 183–190. [[CrossRef](#)]
66. Tang, Q.; Xu, H.; Zheng, Y.; Wang, J.; Li, H.; Zhang, J. Catalytic dehydration of methanol to dimethyl ether over micro-mesoporous ZSM-5/MCM-41 composite molecular sieves. *Appl. Catal. A Gen.* **2012**, *413–414*, 36–42. [[CrossRef](#)]
67. Sun, X.; Mueller, S.; Liu, Y.; Shi, H.; Haller, G.L.; Sanchez-Sanchez, M.; Van Veen, A.C.; Lercher, J.A. On reaction pathways in the conversion of methanol to hydrocarbons on HZSM-5. *J. Catal.* **2014**, *317*, 185–197. [[CrossRef](#)]
68. Zhang, S.; Gong, Y.; Zhang, L.; Liu, Y.; Dou, T.; Xu, J.; Deng, F. Hydrothermal treatment on ZSM-5 extrudates catalyst for methanol to propylene reaction: Finely tuning the acidic property. *Fuel Process. Technol.* **2015**, *129*, 130–138. [[CrossRef](#)]
69. Galanova, E.G.; Magomedova, M.V.; Afokin, M.I.; Starozhitskaya, A.V.; Maximov, A.L. Synthesis of olefins from dimethyl ether in a synthesis gas atmosphere. *Catal. Commun.* **2021**, *153*, 106297. [[CrossRef](#)]
70. Tsaplin, D.E.; Kulikov, L.A.; Maksimov, A.L.; Karakhanov, E.A. Method for Obtaining a Composite material with a Hierarchical Structure. RU Patent 2773945C1, 14 June 2022.
71. Khadzhev, S.N.; Kolesnichenko, N.V.; Gorjainova, T.I.; Birjukova, E.N.; Kulumbegov, R.V. Catalyst and Method of Producing Olefins from Dimethyl Ether in Its Presence. RU Patent 2445158 C2, 20 May 2012.

72. Kolesnichenko, N.V.; Bukina, Z.M.; Jashina, O.V.; Zavalishin, I.N.; Markova, N.A.; Khadzhiev, S.N.; Lin, G.I.; Rozovskij, A.J.; Kitaev, L.E. Catalyst and Method to Manufacture Olefines from Dimethyl Ether in the Presence Thereof. RU Patent 2323777 C1, 10 May 2008.
73. Hubbard, C.R.; Snyder, R.L. RIR—Measurement and Use in Quantitative XRD. *Powder Diffr.* **1988**, *3*, 74–77. [[CrossRef](#)]

Disclaimer/Publisher’s Note: The statements, opinions and data contained in all publications are solely those of the individual author(s) and contributor(s) and not of MDPI and/or the editor(s). MDPI and/or the editor(s) disclaim responsibility for any injury to people or property resulting from any ideas, methods, instructions or products referred to in the content.